applied optics

Analysis of the impact of air scattering on point source transmittance

Zhirui Cao,[1,2] Xianchao Xun,[3] and Yuegang Fu[2,*]

[1]Changchun Institute of Optics, Fine Mechanics and Physics, Chinese Academy of Sciences, Changchun, Jilin 130033, China
[2]Changchun University of Science and Technology, Changchun, Jilin 130033, China
[3]Basic Department, Aviation University of Air Force, Changchun, Jilin 130033, China
*Corresponding author: fuyg@cust.edu.cn

Received 10 April 2018; revised 1 July 2018; accepted 3 July 2018; posted 10 July 2018 (Doc. ID 327782); published 2 August 2018

This paper proposes a method to simulate an average air scattering model by using random particles obeying a certain size spectrum and shape distribution, and it analyzes the influence of air scattering on the point source transmittance (PST) test using the model. The results of the analysis indicated that PST measurement errors caused by air scattering are directly proportional to the cube of the diameter of the optical system and that a one-level change in the air cleanliness may result in a one-order-of-magnitude change in the error. The cleanliness level of the measurement environment is less expensive and easier to obtain from analysis than from empirical values.

https://doi.org/10.1364/AO.57.006664

1. INTRODUCTION

During the point source transmittance (PST) measurement processes, the parallel beam incident from an angle outside the field of view of the system to be measured is scattered by air-suspended particles, and part of the scattered light enters the imaging field of view of the system, resulting in PST test errors. Therefore, during high-precision PST measurement processes, two variables have to be evaluated and controlled: the measurement error due to air scattering and the air cleanliness level of the environment where the measurement is performed. X-ray multi-mirror (XMM) telescopes are able to perform PST measurements with a precision of 10^{-10} in a clean environment that satisfies International Organization for Standardization (ISO) class 3 [1]. Ball Aerospace & Technologies Corp. established a stray light laboratory with an air cleanliness level of ISO class 3, and the PST measurement precision of the operation land imager (OLI) telescope under such environmental conditions achieved an order of 10^{-9} [2–4]. The James Webb Space telescope performed a stray light test under vacuum conditions, and the impact of air scattering was found to be negligible in this case [5].

The Chinese Science Academy is now developing a space telescope similar to the Hubble telescope, whose PST is designed to be less than 4.6×10^{-9} when the off-axis field angle is 45°. Based on previous engineering experiences, the air cleanliness level of the environment chosen to perform the measurement needs to be superior to ISO class 3. Given that the dimensions of the telescope envelope are $8.5 \times 2.7 \times 3.8$ m^3 and that the PST measurement space exceeds 600 m^2, which is far greater than the measurement space of XMM and OLI telescopes, the realization of an ISO class 3 air cleanliness level in such a large space is extremely difficult and very expensive. Thus, widespread suspicions have been raised about the feasibility of implementation of PST measurement by means of this new space telescope. It is essential to avoid unnecessary technical obstructions and waste of investment; for this reason, the impact of air scattering on the PST measurement needs to be quantitatively analyzed to determine the most optimal environmental conditions in which to perform PST measurements.

To ensure a precise quantitative analysis, an accurate air scattering model needs to be implemented. The scattering of airborne particles in the laboratory can be viewed as uncorrelated single scattering, so the scattering properties of particle swarms may be treated as the superposition of the scattering properties of single particles in all sizes (where each particle size is represented by the equivalent spherical diameter) and shapes. Several approaches to describe the scattering properties of single particles are known, such as the Mie theory [6,7], Rayleigh method, Rayleigh–Gans–Stevenson (RGS) method, geometric optics approximation (GOA) method [8–10], T matrix method [11], extended boundary condition method (EBCM) [12], separation of variables method (SVM) [13], point matching method (PMM) [14], method of moments (MoM) [15], discrete dipole approximation (DDA) [16], Fredholm integral equation method (FIEM), finite-difference time-domain (FDTD) method [10], and multi-resolution time-domain (MRTD) method. The MRTD method is a combination of the MoM algorithm and FDTD algorithm. It is a high-order differential expansion of Maxwell and has good numerical

dispersion; compared to the traditional FDTD algorithm, the MRTD method can save computing resources while maintaining accuracy of computation [17]. When the sizes and shapes of the suspended particles are different, it is not practical to list the scattering properties of each particle. Therefore, how to simulate the scattering properties of complex particle swarms simply and accurately is a problem that needs to be studied [18–20].

In this paper, random particles with a certain size spectrum and shape distribution are used to simulate the average scattering properties of the air so that calculation of the synthesized scattering properties of particle swarms is simpler and more accurate.

2. MODELING OF AIR SCATTERING

Air scattering primarily consists of the scattering of gas molecules and suspended particles. However, engineering experience indicates that the impact of the scattering of gas molecules on the PST measurement can be neglected [1–4]. Thus, this paper mainly investigates the scattering properties of air-suspended particles with an equivalent spherical diameter greater than 0.1 μm. Generally, the size spectrum and the shape distribution of suspended particles in air are complicated, and the scattering properties of any type of spherical/non-spherical particles cannot be used to precisely describe the scattering properties of the air particle swarms. We used the MRTD algorithm to calculate the scattering model of non-spherical particles [21], and then we considered random particles with a certain size spectrum and shape distribution to simulate the air scattering model of the laboratory.

The size spectrum distribution of particle swarms indicates that the distributions of the number of particles with different sizes in a unit volume are different. To characterize this phenomenon, we use a size distribution function $f(r)$. The typical laboratory air particle size distribution functions include gamma distributions [22], log-normal distributions [23], and index distributions, and the major parameters of each model may be extracted by fitting experimental data. For a certain $f(r)$, the effective radius r_e and the effective variance ν_e are also given, as shown in Eqs. (1) and (2) [24],

$$r_e = \frac{\int_r \pi r^3 f(r)\mathrm{d}r}{\int_r \pi r^2 f(r)\mathrm{d}r}, \tag{1}$$

$$\nu_e = \frac{\int_r (r - r_e)^2 \pi r^2 f(r)\mathrm{d}r}{r_e^2 \int_r \pi r^2 f(r)\mathrm{d}r}, \tag{2}$$

where r represents the equivalent spherical diameter of the particle.

As specified before, the fact that the number of particles with different shapes in the unit volume is not constant has to be taken into account. From the observation and the statistical analysis of the properties of the shape distribution of the particle swarms, if random particles with m types of typical shapes are used to simulate the scattering model of complex air particle swarms, and each distribution associated to the number of particles with a given shape is represented by the normalized weight coefficient W_k, then,

$$\sum_{k=1}^{m} W_k = 1. \tag{3}$$

Then, we use the Mueller matrix $F(\theta)$ to describe the scattering properties of the particles. Given the relation between $F(\theta)$ and the Stokes matrices of the incident and scattering lights, the Mueller matrix can be written as in the following [25]:

$$\begin{bmatrix} I \\ Q \\ U \\ V \end{bmatrix} = \begin{bmatrix} F_{11}(\theta) & F_{12}(\theta) & 0 & 0 \\ F_{21}(\theta) & F_{22}(\theta) & 0 & 0 \\ 0 & 0 & F_{33}(\theta) & F_{34}(\theta) \\ 0 & 0 & F_{43}(\theta) & F_{44}(\theta) \end{bmatrix} \times \begin{bmatrix} I_0 \\ Q_0 \\ U_0 \\ V_0 \end{bmatrix}, \tag{4}$$

where θ is the scattering angle; I_0, Q_0, U_0, and V_0 are the Stokes matrix elements of the incident light; and I, Q, U, and V are the Stokes matrix elements of the scattering light. The value of each Mueller matrix element is inversely proportional to the square of the distance l between the scattering particle and the scattering observation point.

The calculation method of the Mueller matrix element, after having been averaged by using the size spectrum and shape distribution, has the following expression:

$$\overline{F_{11}} = \frac{\sum_{k=1}^{m} W_k \int_r F_{11}(\varepsilon_k, r) K_{\mathrm{sca}}(\varepsilon_k, r) S_P(\varepsilon_k, r) f(r)\mathrm{d}r}{\sum_{k=1}^{m} W_k \int_r K_{\mathrm{sca}}(\varepsilon_k, r) S_P(\varepsilon_k, r) f(r)\mathrm{d}r}. \tag{5}$$

In Eq. (5), all terms indexed with k refer to a group of particles with a certain shape. In more detail, $\overline{F_{11}}$ represents the head element of the Mueller matrix after having averaged the air particle swarms by size spectrum and shape distribution; $F_{11}(\varepsilon_k, r)$ is one head element of the Mueller matrix corresponding to the particles with a certain shape, $K_{\mathrm{sca}}(\varepsilon_k, r)$ is the scattering coefficient, $S_P(\varepsilon_k, r)$ indicates the geometric projection area of particles along the light transmission direction, ε_k represents the shape parameter, and W_k is the weight coefficient of typical particles in a certain shape. Obviously, the calculation method of other Mueller matrix elements, corresponding to particles with a different shape than the one indicated by k, has the same mathematical expression as Eq. (5). The solution of W_k is based on the least-squares principle. That is, the value of W_k is determined so that the sum of the variance of the elements corresponding to the Stokes matrices of incident and emergent light is minimal, as shown in the following:

$$\mathrm{MIN}(S) = \sum_{\theta} \left(\frac{I - \overline{F_{11}(\theta)} I_0 - \overline{F_{21}(\theta)} Q_0}{I} \right)^2. \tag{6}$$

In Eq. (6), the scattering light intensity is obtained experimentally, and the Stokes matrix elements of the incident light are determined by the polarization state of the incident light [3].

3. MODELING OF PST MEASUREMENT ERROR CAUSED BY AIR SCATTERING

In a certain measurement wave band, the PST is defined as the ratio between the irradiance $E_d(\theta)$ and the irradiance E_i. The irradiance $E_d(\theta)$ is generated at the optical system image surface by the point source target at the off-axis viewing angle θ, and the irradiance E_i is generated at the entrance of the optical system. The corresponding mathematical expression is

$$\mathrm{PST}(\theta) = \frac{E_d(\theta)}{E_i}. \tag{7}$$

The PST measurement optical path of the to-be-measured system [26–28] is shown in Fig. 1, where the diameter of the light path of the system is D, the field angle is 2ω, and the PST measurement field angle is α. The grid in the figure indicates the overlapping region between the object view of the to-be-measured system and the light beam of the PST measurement, and the suspended particles within this region scatter the measurement light beam. When the scattering angle θ is in the range $[\alpha - \omega, \alpha + \omega]$ and the orientation angle φ is in the range $[-\omega, +\omega]$, the scattering light enters the image-forming field of the to-be-measured system and directly affects the precision of the PST measurement.

The laboratory air scattering is treated as an uncorrelated single scattering, and, correspondingly, the synthesized scattering strength of the air particle swarms is equal to the mathematic superposition of the scattering strengths of all particles. If the average air scattering light intensity $I(\theta)$ is known, the irradiance E generated by the scattering light on the image surface of the to-be-measured system is expressed as

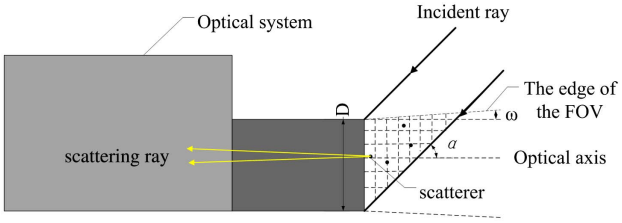

Fig. 1. Schematic view of PST measurement optical path and primary scattering region.

$$E = V \times N \times \int_{-\omega}^{\omega} \int_{\alpha-\omega}^{\alpha+\omega} I \sin\theta l^2 \mathrm{d}\theta \mathrm{d}\varphi. \tag{8}$$

In Eq. (8), $V \approx \pi D^3/8 \tan\alpha$ is the volume of the grid region in Fig. 1. N is the concentration of the scattering particles, and it is calculated based on the maximum value of the air cleanliness division standards, as seen in Table 1; l is the distance between the scattering particles and the scattering observation point.

4. QUANTITATIVE ANALYSIS AND VALIDATION RESULTS

A. Statistics of Size and Shape Distributions of Air Particles

We measured the size distributions of particle swarms under ISO Class 8, ISO Class 7, and ISO Class 6 by using an air particle counter. The air pump continuously draws in air containing suspended particles from the sampling air path. When the sampling air is drawn through the laser scattering cavity, the laser is scattered by the suspended particles, and the scattered light converges on the photodetector through the condenser lens. The signal processing system calculates the number of suspended particles per unit volume of sampling air based on the count of electrical pulses and determines the sizes of the particles based on the intensity of the electrical pulse signal. The results are shown in Fig. 2, where the y axis represents the particle concentration for particles equal to and larger than the considered sizes.

The experimental results indicate that the concentration of air particles changes according to the cleanliness level. However, the shape distributions of air particle swarms under different cleanliness levels were almost consistent among each other, and the characteristics of the size spectra were almost the same, regardless of the ISO standard considered. The size distribution function $f(r)$ roughly satisfied the index distribution indicated by

$$\frac{\int_{r_1}^{\infty} f(r)\mathrm{d}r}{\int_{r_2}^{\infty} f(r)\mathrm{d}r} = \left(\frac{r_1}{r_2}\right)^{-n}, \tag{9}$$

where the distribution index is $n = 2.08$.

We observed the deposition test strips of air particles under ISO Class 8, ISO Class 7, and ISO Class 6 by microscopy; the deposition test strips are placed in different positions in

Table 1. Standards of Air Cleanliness Class[a]

	Maximum Concentration Limits (pc/m3 of air)					
	$d \geq$					
ISO Classification Number (N)	0.1 μm	0.2 μm	0.3 μm	0.5 μm	1 μm	5 μm
ISO class 1	10	2				
ISO class 2	100	24	10	4		
ISO class 3	1000	237	102	35	8	
ISO class 4	10000	2370	1020	352	83	
ISO class 5	100000	23700	10200	3520	832	29
ISO class 6	1000000	237000	102000	35200	8320	293
ISO class 7				352000	83200	2930
ISO class 8				3520000	832000	29300

[a]The symbol d indicates the particle size.

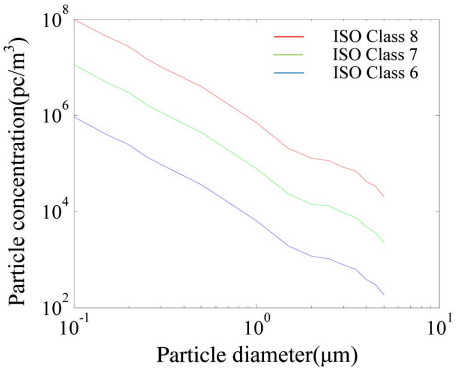

Fig. 2. Measured data of the air particle size distribution.

the laboratory, the observation work is carried out several times at different times, and the shape distributions of air particles are based on a large number of observations. The observation results show that the shape distributions of air particles were almost identical under different cleanliness levels, and the air particles in the lab mostly had ellipsoidal and cylindrical shapes, as Fig. 3 shows. Thus, we considered ellipsoidal particles in 10 random shapes and cylindrical particles in 10 random shapes to simulate the scattering properties of the air particle swarms.

The shape of the ellipsoidal particles was represented by an aspect ratio of a/b, and the shape of the cylindrical particles was represented using the diameter-to-length ratio D/L, as shown in Fig. 4. The aspect ratio of the ellipsoidal particles had a uniform distribution in the range [0.3,3.0], which we divided into 10 equal intervals; the diameter-to-length ratio of the cylindrical particles was evenly distributed in the range [0.05,1.0] and divided into 10 equal intervals.

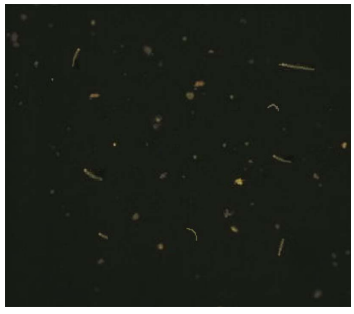

Fig. 3. Sediments of air-suspended particles observed using the microscope.

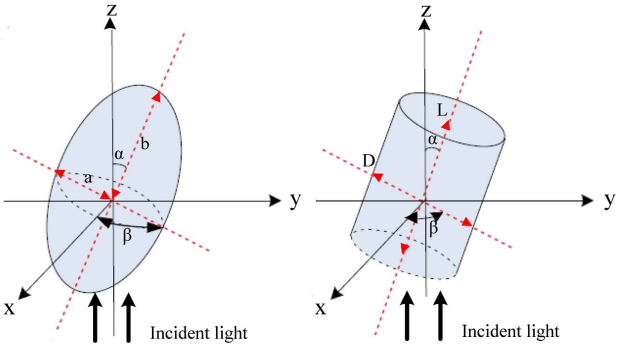

Fig. 4. Illustration of parameters of ellipsoidal and cylindrical particles.

B. Solution and Verification of the Scattering Model

In order to determine the unknown parameters in Eq. (5), we performed an optical path test, as shown in Fig. 5 [28]. The experimental setup was located in a dark room with an air cleanliness level below IS0 class 8 and it included a pulse laser, an optical collimated system with a diameter of 100 mm, and a photoelectric detector with supporting and adjusting mechanisms and a light trapping mechanism. The polarization of the emergent, 0.47-μm-wavelength laser light was adjusted via a polarization plate such that the Stokes matrix was normalized into the matrix (1, 1, 0, 0)T. In addition, the usage of the light trapping mechanism was crucial to prevent the light beam from being scattered back by the inner wall of the laboratory to the measurement region, thus making the measurement precision worse.

In the scattering angle range of [5°, 175°], the light intensity I was measured every 2.5°, the average distance from the measurement point to the scattering particles was $r = 1$ m, and all the measured data were normalized based on the intensity of the incident light I_0, as illustrated in Fig. 6.

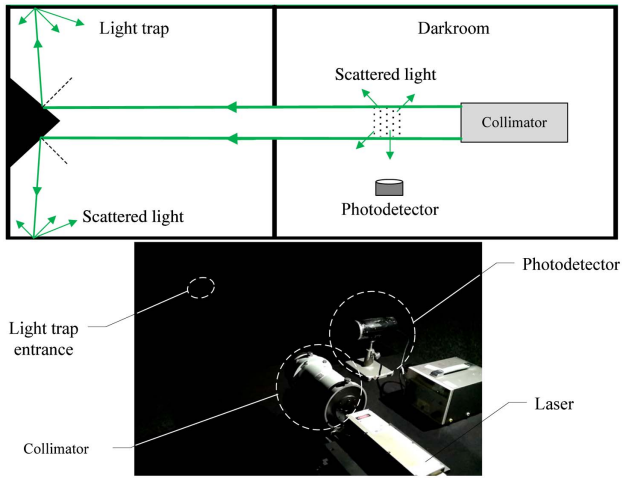

Fig. 5. Model for optical path verification.

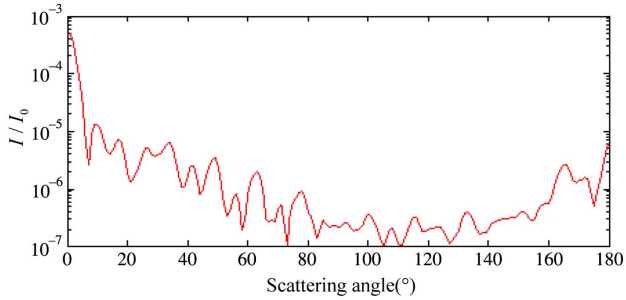

Fig. 6. Measurement data of the scattering light intensity.

Starting from these measured data, the average Mueller matrix elements of the air were calculated by averaging the particle size spectrum and shape distribution; then, the average Mueller matrix elements were compared with the Mueller matrix elements of the equivalent spherical particles calculated by using the Mie scattering theory. The results are shown in Fig. 7.

As can be noted from Fig. 7 (top right), the Mueller matrix element $\overline{F_{11}}$ obtained by averaging the size spectrum and shape distribution is smaller than the Mie scattering result along the forward-scattering direction, whereas the former is greater than the latter along the backward-scattering direction. In some cases, the calculation results of other Mueller matrix elements were significantly different with respect to the Mie scattering calculation results. For example, the sign of the average calculation result of $\overline{F_{12}}/\overline{F_{11}}$ (Fig. 7 top right) was nearly opposite to that of the Mie scattering result; the average calculation result of $\overline{F_{22}}/\overline{F_{11}}$ (Fig. 7 middle left) varied significantly according to the scattering angle, whereas the Mie scattering calculation result remained constant at 1.0. In summary, the average scattering properties of the air particle swarms greatly differed from the Mie calculation results.

To validate the accuracy of the calculation results of the average Mueller matrix, we calculated the scattering light intensities according to two different approaches: 1) the Mueller matrix obtained by applying the averaging and 2) the Mueller matrix obtained by applying the Mie scattering theory. The results obtained are reported in Fig. 8, together with the measurement results.

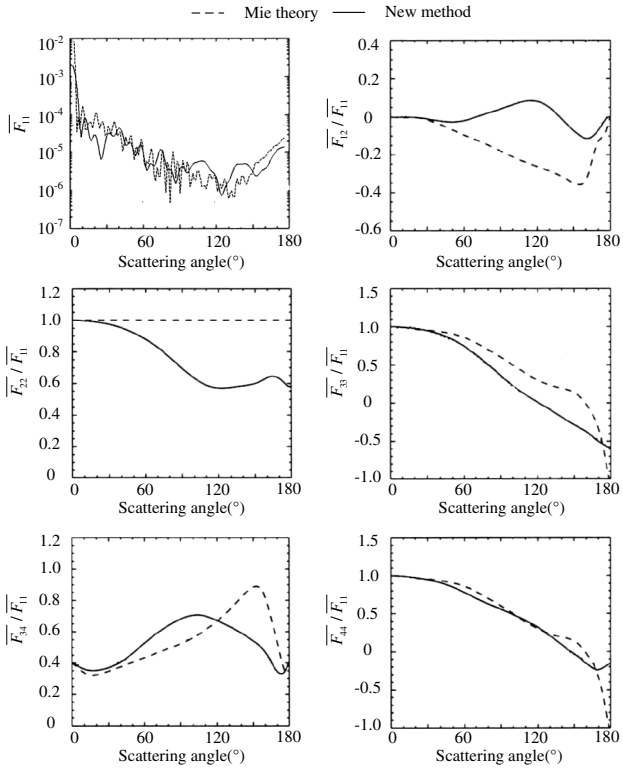

Fig. 7. Mueller matrices of single air particles and equivalent spherical particles obtained by averaging the size spectrum and the shape distribution.

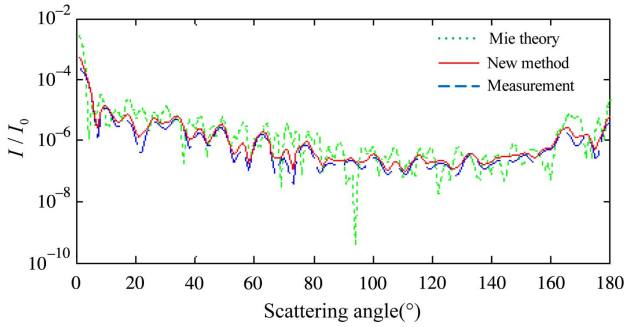

Fig. 8. Comparison between the scattering light intensities obtained using different algorithms and the measured data.

As can be observed from Fig. 8, the maximum deviation between the measurement results and the air scattering model obtained by calculation (i.e., averaging the particle size spectrum and shape distribution) was less than 12%, whereas the average deviation between the measurement result and the calculation result of the traditional Mie scattering model exceeds 480%, which sufficiently demonstrates the precision advantage of the air scattering model proposed in this paper.

C. Quantitative Analysis and Verification of the Errors Caused by Air Scattering

As far as the to-be-measured optical system is concerned, the chosen parameters in this paper are: $D = 2$ m, $2\omega = 1.5°$, $\alpha = 45°$, wavelength λ of the incident light equal to 0.47 μm, $I_0 = 1$ lux, and irradiance of incident light equal to 1 W/m^2. Based on the characteristics of the size spectrum and the shape distribution described above, the irradiance caused by the air scattering at the image surface of the to-be-measured system was calculated under different air cleanliness levels, as indicated in Table 2. The calculation results were numerically equal to the PST measurement errors caused by the air scattering.

To validate the accuracy of the quantitative analysis results, the test optical path shown in Fig. 9 was set up in a dark room where the air cleanliness level could be controlled. The major test devices included a to-be-measured system with a scaled-down design, a measurement light source, a measurement optical collimation system, and a photo-electric detector with its supporting and adjusting mechanisms and light trapping mechanism. The diameter of the to-be-measured system was 500 mm, and when the incident angle of the scattering light was greater than or equal to 45°, the PST was designed to be less than 5.9×10^{-9}; the light source was a pulse laser with an emergent light wavelength of 0.47 μm; and the measurement optical collimation system consisted of parallel light tubes with a diameter of 700 mm. The measurement beam entered at a field angle of 45°, thus passing in front of the entrance of the to-be-measured system and then entering into the light trapping system. In this way, the light beam was not scattered by the inner wall of the laboratory into the measurement region, thus avoiding any impact on the measurement precision. Finally, the S5973 photodiode of the Hamamatsu Corporation was used as the detector to measure the irradiance E_1 of the beam and the irradiance E_2 at the image surface of the to-be-measured system. The quantum efficiency of the detector is about

Table 2. Irradiance of Air Scattering Generated at the Image Surface of the to-be-Measured System for Different Air Cleanliness Levels

ISO Air Cleanliness Level	Class 3	Class 4	Class 5	Class 6	Class 7	Class 8
Surface irradiance (W/m^2)	5.6×10^{-13}	5.6×10^{-12}	7.2×10^{-11}	7.2×10^{-10}	7.2×10^{-9}	7.2×10^{-8}

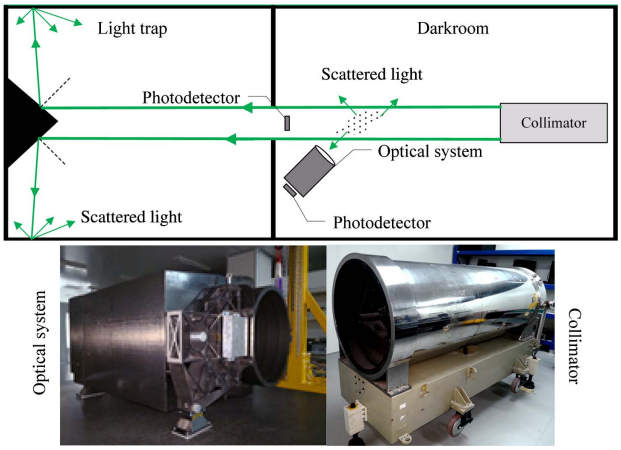

Fig. 9. Schematic view of the test optical path.

91%, the maximum value of the dark current is about 70 pA, and the detector's photosensitive diameter is 0.4 mm (the focus lens with a diameter of 2 mm in front of the detector). The radiometric calibration results of the detector show that for the 1×10^{-6} W/m^2 optical radiation signal, when the integration time is 20 s, the SNR is larger than 12.

After the stabilization of the air cleanliness level of the laboratory at ISO class 8 and ISO class 7, the PST measurement error σ caused by air scattering was calibrated, and the measurement error was calculated as

$$\sigma = \frac{E_2 - E_0}{E_1 - E_0}, \tag{10}$$

where E_0 is the noise of the dark current of the photoelectric detector. The calibration and the analysis results of the PST measurement error σ caused by air scattering are shown in Table 3.

By comparing the calibration results with the analysis results, it can be observed that the lower the air cleanliness level, the smaller the absolute deviation between calibration and analysis. When the air cleanliness level is at ISO class 7, the absolute deviation between calibration and analysis is approximately 0.5×10^{-10}.

5. CONCLUSIONS

Based on the existing non-spherical particle scattering model, in this paper we considered random particles obeying a certain size spectrum and shape distribution to simulate the average air scattering model. The method proposed provides an easy and feasible processing approach to precisely obtain the scattering properties of complex particle swarms. The maximum relative error between the measured results and the air scattering model obtained by this solution was less than 12%.

The average air scattering model was applied to quantitatively analyze the impact of the air scattering on the PST measurements, and when the air cleanliness level was superior to ISO class 7, the error of the quantitative analysis was smaller than 0.5×10^{-10}. The analysis results indicate that the PST measurement error caused by air scattering is directly proportional to the cube of the diameter of the to-be-measured optical system. In addition, we observed that every time the air cleanliness is upgraded or degraded by one level, the PST measurement error may increase or decrease by 1 order of magnitude, respectively. Last, in order to satisfy an order of 10^{-9} for the PST index verification of the to-be-measured system with a diameter of 2 m, the cleanliness level of the measurement environment needs to be superior to ISO class 6, which is three levels lower than the empirical environmental conditions. According to experience, establishing an ISO class 3 clean room requires an additional ISO class 6 clean room for transition, which will result in a million dollars in wasted money.

The air scattering model established in this paper had good accuracy because the shapes of the air particles that were studied were relatively concentrated and the rationality of random particle shape and number selection was relatively low. For particles with a complex shape distribution, how to choose the shapes and quantities of random particles is a subject that needs further study and practice.

Table 3. Comparison between the Calibration Result and the Analysis Result

Air Cleanliness Level	ISO Class 7	ISO Class 8
E1-E0 measurement result (W/m^2)	1.3×10^{4}	1.3×10^{4}
E2-E0 measurement result (W/m^2)	0.89×10^{-6}	1.08×10^{-5}
E2-E0 analysis result by the average air scattering model (W/m^2)	1.43×10^{-6}	1.43×10^{-5}
E2-E0 analysis result by Mie scattering (W/m^2)	4.94×10^{-6}	4.94×10^{-5}
σ calibration result	0.67×10^{-10}	0.83×10^{-9}
σ analysis result by the average air scattering model	1.1×10^{-10}	1.1×10^{-9}
σ analysis result by Mie scattering model	3.8×10^{-10}	3.8×10^{-9}

Funding. National Natural Science Foundation of China (NSFC) (61705223).

REFERENCES

1. C. Wührer and R. Birkl, "PST measurements and wide angle straylight analyses of the XMM (X-Ray Multi Mirrror) telescopes," Proc. SPIE **4012**, 113–122 (2000).
2. F. Grochocki and J. Fleming, "Stray light testing of the OLI telescope," Proc. SPIE **7794**, 77940W (2010).
3. J. Fleming, F. Grochocki, and T. Finch, "New stray light test facility and initial results," Proc. SPIE **7069**, 70690O (2008).
4. J. C. Kemp, J. L. Stauder, O. Ames, and S. Turcotte, "Terrestrial black hole for measuring high-rejection off-axis response," Proc. SPIE **3122**, 45–56 (1997).
5. T. Whitman, "Testing a critical stray light path of the James Webb space telescope," Proc. SPIE **7731**, 77310L (2010).
6. K. N. Liou, *An Introduction to Atmospheric Radiation* (Academic, 2003).
7. K. N. Liou, Y. Takano, and P. Yang, "Intensity and polarization of dust aerosols over polarized anisotropic surfaces," J. Quant. Spectrosc. Radiat. Transfer **127**, 149–157 (2013).
8. P. Yang, K. N. Liou, L. Bi, C. Liu, B. Yi, and B. A. Baum, "On the radiative properties of ice clouds: light scattering, remote sensing, and radiation parameterization," Adv. Atmos. Sci. **32**, 32–63 (2015).
9. M. I. Mishchenko, J. W. Hovenier, and L. D. Travis, *Light Scattering by Nonspherical Particles, Theory, Measurements, and Application* (Academic, 2000).
10. P. Yang and K. N. Liou, "Light scattering by hexagonal ice crystals: comparison of finite-difference time domain and geometric optics models," J. Opt. Soc. Am. A **12**, 162–176 (1995).
11. M. I. Mishchenko and L. D. Travis, "Capabilities and limitations of a current FORTRAN implementation of the T-matrix method for randomly oriented, rotationally symmetric scatterers," J. Quant. Spectrosc. Radiat. Transfer **60**, 309–324 (1998).
12. L. Bi and P. Yang, "Tunneling effects in electromagnetic wave scattering by nonspherical particles: a comparison of the Debye series and physical-geometric optics approximations," J. Quant. Spectrosc. Radiat. Transfer **178**, 93–107 (2016).
13. N. V. Voshchinnikov and V. G. Farafonov, "Optical properties of spheroidal particles," Astrophys. Space Sci. **204**, 19–86 (1993).
14. H. M. Al-Rizzo and J. M. Tranquilla, "Electromagnetic scattering from dielectrically coated axisymmetric objects using the generalized point-matching technique (GPMT). II. Numerical results and comparison," J. Comput. Phys. **119**, 356–373 (1995).
15. R. F. Harrington, *Field Computation by Moment Methods* (Macmillan, 1968).
16. B. T. Draine, "The discrete-dipole approximation and its application to interstellar graphite grains," Astrophys. J. **333**, 848–872 (1988).
17. E. M. Tentzeris, A. Cangellaris, and L. P. B. Katehi, "Multiresolution time-domain (MRTD) adaptive schemes using arbitrary resolutions of wavelets," IEEE Trans. Microwave Theory Tech. **50**, 510–516 (2003).
18. M. I. Mishchenko, "Calculation of the amplitude matrix for a nonspherical particle in a fixed orientation," Appl. Opt. **39**, 1026–1031 (2000).
19. X. Li and Z. Chen, "Equiphase-sphere approximation for analysis of light scattering by arbitrarily shaped nonspherical particles," Appl. Opt. **43**, 4497–4505 (2004).
20. T. Rother, K. Schmidt, J. Wauer, V. Shcherbakov, and J.-F. Gayet, "Light scattering on Chebyshev particles of higher order," Appl. Opt. **45**, 6030–6037 (2006).
21. X. Wei, E. Li, and C. Liang, "A new MRTD scheme based on Coifman scaling functions for the solution of scattering problems," IEEE Microwave Wireless Compon. Lett. **12**, 392–394 (2002).
22. J. E. Hansen and L. D. Travis, "Light scattering in planetary atmospheres," Space Sci. Rev. **16**, 527–610 (1974).
23. R. J. Perry, A. J. Hunt, and D. R. Huffman, "Experimental determinations of Mueller scattering matrices or nonspherical particles," Appl. Opt. **17**, 2700–2710 (1978).
24. X. Sun and H. Ha, "Retrieval of the optical thickness and effective radius of aerosols from reflected solar radiation measurements," Acta Phys. Sin. **57**, 5565–5570 (2008).
25. H. C. van der Hulst, *Light Scattering by Small Particles* (Dover, 1981).
26. G. Wang, F. Xing, and M. Wei, "Rapid optimization method of the strong stray light elimination for extremely weak light signal detection," Opt. Express **25**, 26175–26185 (2017).
27. G. Wang, F. Xing, and M. Wei, "Optimization method of star tracker orientation for sun-synchronous orbit based on space light distribution," Appl. Opt. **56**, 4480–4490 (2017).
28. M. Wei and F. Xing, "A real-time detection and positioning method for small and weak targets using a 1D morphology-based approach in 2D images," Light Sci. Appl. **7**, 18006 (2018).